Monitoring contractility in cardiac tissue with cellular resolution using biointegrated microlasers

Schubert, Marcel; Woolfson, Lewis; Barnard, Isla R. M.; Dorward, Amy M.; Casement, Becky; Morton, Andrew

Published in:
Nature Photonics

DOI:
10.1038/s41566-020-0631-z

Publication date:
2020

Document Version
Peer reviewed version

Monitoring contractility in cardiac tissue with cellular resolution using bio-integrated microlasers

Marcel Schubert[1,*], Lewis Woolfson[1], Isla RM Barnard[1], Amy M Dorward[2], Becky Casement[1], Andrew Morton[1], Gavin B Robertson[2], Paul L Appleton[3], Gareth B Miles[4], Carl S Tucker[5], Samantha J Pitt[2], Malte C Gather[1,6*]

[1] SUPA, School of Physics and Astronomy, University of St Andrews

[2] School of Medicine, University of St Andrews

[3] School of Life Sciences, University of Dundee

[4] School of Psychology & Neuroscience, University of St Andrews

[5] The Queen's Medical Research Institute, University of Edinburgh

[6] present address: Centre for Nanobiophotonics, Department of Chemistry, Universität zu Köln

* ms293@st-andrews.ac.uk; mcg6@st-andrews.ac.uk

The contractility of cardiac cells is a key parameter describing the bio-mechanical characteristics of the beating heart, but functional monitoring of 3D cardiac tissue with single cell resolution remains a major challenge. Here, we introduce microscopic whispering gallery mode (WGM) lasers into cardiac cells to realize all-optical recording of transient cardiac contraction profiles with cellular resolution. The brilliant emission and high spectral sensitivity of microlasers to local changes in refractive index enable long-term tracking of individual cardiac cells, monitoring of drug administration, accurate measurements of organ scale contractility in live zebrafish, and robust contractility sensing through hundreds of micrometres of rat heart tissue. Our study reveals changes in sarcomeric protein density as an underlying factor to cardiac contraction. More broadly, the use of novel micro and nanoscopic lasers as non-invasive, bio-integrated optical sensors brings new opportunities to monitor a wide range of physiological parameters with cellular resolution.

An estimated 26 million patients suffer from heart failure worldwide, and further advances in cardiac regeneration depend critically on the ability to locally resolve the contractile properties of heart tissue[1,2]. Currently available techniques lack speed, sensitivity and single cell specificity, especially in deep tissue. To monitor cardiac contractility in isolated cells in a culture dish, transmission or fluorescence microscopy is often sufficient to track the distinct structural features of myofibrils[3], cellular organelles which comprise repeating contractile elements called sarcomeres. However, characterising contractility with adequate resolution in the more complex 3-dimensional structures of cardiac tissue remains a major challenge, both *in vitro* and *in vivo*, mainly due to the fast dynamics of contractions (<50 ms), the strong motion of the tissue and the severe scattering of light in tissue. Force transducers or soft strain gauge sensors have been developed, but their spatial resolution is very limited[4]. In transparent zebrafish, light sheet microscopes in combination with image reconstruction algorithms allow volumetric imaging of whole hearts with single cell resolution.[5] However, their resolution is too low to extract the contractility of single cells as this requires tracking nanometre changes in sarcomere spacing[2]. To achieve this resolution, fast intravital scanning confocal or multiphoton microscopes have been developed but the need for extensive image artefact removal by retrospective gating, active tissue stabilisation, and targeted fluorescent labelling means that so far they can only extract averaged contraction profiles. In addition, due to the inherent tissue dynamics, progress in achievable imaging depth has stalled at less than 100 µm from the heart surface[1,2,6,7], in strong contrast to functional imaging of the brain which has recently reached a depth of 850 µm[8].

To elucidate CM contractility under various experimental conditions, we explored the integration of WGM microlasers as multifunctional optical sensors. Chip-based fibre- and prism-coupled WGM biosensors have previously achieved sensitivities down to the single molecule and protein level[9,10].

However, their potential for intracellular sensing remains largely unexplored as integration into biological systems requires further miniaturization, self-sustained and prolonged emission of light, and data analysis protocols with improved robustness. Recently, microlasers were proposed as novel optical tags to uniquely discriminate hundreds of thousands of cells[11–15].

Intracellular refractive index sensing

Fig. 1 illustrates the general principle of our laser-based contraction sensor. Brightly fluorescent polystyrene microspheres with a diameter between 10 and 20 µm were used as efficient and robust microscopic WGM lasers that show multi-mode emission under remote optical pumping[11]. These lasers were actively internalized by different types of cardiac cells (Supplementary Fig. 1). Upon CM contraction, individual peaks in the emission spectrum of the lasers showed a spectral red-shift (typically, $\Delta\lambda \approx 50$ pm; Fig. 1d). Due to the bright and narrowband laser emission, the wavelength of each lasing mode can be monitored rapidly (acquisition rate, 100 Hz) and accurately (spectral resolution, 1 pm), revealing pulse-shaped perturbations in lasing wavelength synchronized across all modes and coincident with the spontaneous contractions of the cell (Figs. 2a, 2b and Supplementary Video 1). By tracking at least 2 pairs of TE and TM lasing modes and fitting their position to an optical model, we independently determined the diameter *D* of each microsphere and the average external refractive index n_{ext}, i.e. the refractive index (RI) of the volume probed by the evanescent component of the WGM (Fig. 2c, Supplementary Fig. 2 and Supplementary Information). This revealed a characteristic increase in RI during cell contractions. Statistical analysis of the microsphere diameter was then applied to reduce the effect of fitting noise before reiterating the RI calculation. This significantly improved the signal quality and thus allowed the detection of minute changes in n_{ext}, with a RI resolution of 5×10^{-5} (Supplementary Information), which rivals the most sensitive cell refractometric techniques currently available[16].

Of the 2 pairs of TE and TM lasing modes required for fitting to the optical model, the brightest mode typically has a lasing threshold well below 1 mJ/cm² (corresponding to <1 nJ/pulse, Fig. 2d). Above threshold, this mode rapidly increased in intensity to become orders of magnitude more intense than the background, which is mostly formed by bulk fluorescence of the microlaser (signal-to-background ratio, SBR > 15dB). Single pulse excitation at around 1-2 mJ/cm^2 can be therefore used to accurately determine the spectral position of this mode (Supplementary Fig. 3). By comparison, the least intense mode of the 2 pairs required 10 to 50 times higher pump energy to pass the lasing threshold and to determine its spectral position with sufficient accuracy to ensure convergence of our fitting algorithm. Furthermore, we found that the periodic changes in RI due to cardiomyocyte contraction can be utilized to determine the sensitivity (*S*) of each laser mode (Fig. 2e, Supplementary Fig. 4). Using *S* and tracking the spectral position of just the brightest lasing mode

then allows calculation of a linearly approximated external refractive index n_{ext}^{*}, reducing the minimum required pump energy by at least one order of magnitude. This calibration protocol enabled real time RI sensing, allowed continuous yet non-disruptive read-out (Fig. 2f) and greatly improved the robustness of the approach under challenging experimental conditions (see below).

Analysis of multiple CMs furthermore revealed that contractions consistently led to an increase of cellular RI which indicates the presence of a reproducible physiological process that alters the optical properties of CMs depending on the activation state of their contractile elements (Fig. 2g).

Microlasers monitor myofibril contractility

To identify the origin of the RI increase during CM contraction, we analysed the 3D organization of myofibrils. It is generally assumed that CMs contract under isovolumetric conditions[17], yet X-ray diffraction experiments have revealed a linear relationship between sarcomere length and volume of the myofibril unit cell indicating that cell contractions significantly increase the protein density of the myofibrils[18]. 3D reconstructions of cells showed that microlasers are surrounded by and in direct contact with a dense network of myofibrils (Figs. 3a and 3b, Supplementary Fig. 5), indicating a strong overlap of the contractile protein machinery with the evanescent field of the laser mode, which typically extends up to 200 nm above the resonator surface. Cellular contractility in neonatal CMs was then measured by staining sarcomeric actin filaments and tracking their length change during the contraction cycle, while simultaneously recording spectral shifts in microlaser emission (Figs. 3c and 3d, and Supplementary Video 2). We find that the shortening in the sarcomere length (SL) of myofibrils was linearly correlated to n_{ext} (Supplementary Fig. 6). In contrast, we did not observe spectral shifts for microlasers located inside CMs that were not actively beating even when these were in direct contact with a contracting neighbouring cell, confirming the very localized nature of evanescent field sensing. This indicates that structural changes inside contracting myofibrils cause the red-shift in lasing wavelength. Given that during systole n_{ext} increased by up to 0.003 and using the known protein refractive index increment (dn/dc), we further estimated that the observed contraction-induced changes in sarcomere length by about 10% led to a maximum increase in protein concentration of approximately 8% (Supplementary Information). This finding is consistent with the previously reported decrease in unit cell volume[18]. It does not contradict observations that the contraction of the whole heart is isovolumetric; during contraction, cardiac cells are likely to expel water from the myofibrils into different parts of the cell or to the extracellular space[19], causing a local increase in myofibril density while still conserving the overall tissue volume. The effects associated with sarcomeric lattice spacing and unit cell changes are of great importance for the function of cardiac cells and are believed to play an important role in regulating the length-dependent activation of the heart (Frank-Starling law). Since transient RI

profiles provide a direct measure of CM contractility and myofibril density, they provide new insights to the mechano-biology of cardiac cells. Importantly, the signal monitored by the microlaser closely matches the contractility dynamics of nearby cells (Supplementary Fig. 7, Supplementary Video 3) indicating that the functional properties of neonatal CMs are not affected by the presence of the microlasers.

Single cell barcoding

As the microlaser size provides a unique label to identify and track individual cells over time (Supplementary Fig. 8)[11], we were able to perform repeated monitoring of single neonatal CMs (Fig. 4a). Normalized contractility profiles (Fig. 4b) showed high temporal regularity with minimal beat-to-beat variations in pulse width (FWHM, Fig. 4c) and contraction time (t_{con}, Fig. 4d). For the example in Fig. 4a, after 42 h, we observe the spontaneous transition into tachycardia which is typically accompanied by increased myocardial tension at elevated beating rates (Bowditch effect), a fundamental process underlying the force-frequency relationship of the heart[20]. At the cellular level, this is caused by increased contractility, which we detected as a step-like increase in the maximum and baseline n_{ext} (black arrow in Fig. 4a), allowing simple quantification of relative protein density changes during the entire contraction cycle.

Monitoring drug administration

Next, we used the quantitative RI transient provided by our laser sensors to assess the effect of the calcium channel blocker nifedipine (Fig. 4e). While the effect of nifedipine on voltage-gated Ca^{2+}-channels and subsequent intracellular Ca^{2+} dynamics is well documented[21,22], the effect on contractility is less well understood as it is difficult to access in neonatal and iPS-derived cardiomyocytes. After administration of nifedipine and following a short period of adaptation, spontaneously beating neonatal CMs showed strongly reduced contraction and relaxation speeds (Fig. 4f,g). Furthermore, while we observed that nifedipine increased the pulse-to-pulse variability in Δn_{ext}, the time to reach the maximum contraction changed only marginally (Fig. 4f). The lower contraction speed was therefore largely caused by a reduced contractility of the cell. Under these compromised conditions, the relationship between the mechanical dynamics (contraction speed) and the maximum density change a cell can produce ($\Delta n_{\mathrm{ext,\,max}}$) was linear (Fig. 4h, Supplementary Fig. 9). The nanoscopic probe volume of microlasers and the quantitative contractility information they provide therefore offer insights into fundamental bio-mechanical processes of cardiac cells, e.g. revealing links between contractility, cross-bridge formation and mechano-transduction in individual myofibrils (Supplementary Fig. 9).

Simultaneous sensing of Calcium dynamics and contractility

Microlaser contractility measurements can also be combined with all-optical electrophysiology platforms[21,22]. Simultaneous laser spectroscopy and calcium imaging were performed on fully differentiated mouse CMs that comprise highly organized myofibrils and a transverse tubular system ensuring synchronized calcium release and rapid contraction throughout the cell (Figs. 5a and 5b, Supplementary Video 4). Being non-phagocytic, adult CMs are not able to actively internalise microlasers; so we instead measured spectral changes in the emission of microlasers that were in contact with the cell membrane. Transient profiles of single adult CMs again showed contractions as periodic increases in RI, albeit with smaller amplitude than before (Fig. 5c, Supplementary Fig. 10), demonstrating that Δn_{ext} depends on the volume overlap of the evanescent component of the lasing mode with the myofibrils. However, consistent with our previous observation, the RI transient showed a direct correlation with sarcomere length (Fig. 5c), confirming a contraction-induced change in myofibril density. We also compared the contractility profile to the profile of cytosolic Ca^{2+} and found a characteristic latency time of 30 ms between calcium signalling and force development while the maximum contraction speed coincided with peak Ca^{2+} concentration (Fig. 5c).

***In vivo* integration**

Having demonstrated intra- and extracellular sensing *in vitro*, we next implemented our technique in live zebrafish, a model organism with remarkable capabilities to repair and regenerate large fractions of the heart[23]. Microlasers were injected by a microneedle (Fig. 5d), placing them at the outer wall of the atrium (Figs. 5e and 5f). Extracellular sensing rather than direct intracellular injection was performed to avoid disruption of the myocardium which at this developmental stage consists of a single layer of cardiomyocytes that is not yet covered by the developing epicardium[24,25]. Lasing wavelengths again showed the typical red-shift associated with cardiomyocyte contraction (Supplementary Fig. 11). Due to increased tissue scattering and rapid movement (Supplementary Video 5), the intensity of individual modes varied strongly, and the lower intensity TM modes were not detected for a large fraction of the contraction cycle. However, after calibrating the sensitivity of the microlaser from time-points that contained a sufficient number of modes (Supplementary Fig. 12; c.f. Fig. 2d), we were able to construct complete contractility profiles for the beating zebrafish heart (Fig. 5g). A measurement performed at a more posterior position of the atrium revealed a significantly longer systolic plateau (Supplementary Fig. 13), demonstrating locally resolved contractility profiles under *in vivo* conditions.

Deep tissue contractility sensing

Scattering of light in biological tissue severely limits the maximum depth at which optical imaging and sensing can be performed. To explore the advantages of microlasers over conventional fluorescent probes for deep tissue recording, we performed contractility sensing in preparations of

thick, electrically paced myocardial slices (Fig. 6a). With the ability to maintain functional, contractile heart sections for several months, cardiac slices represent an increasingly important model system for drug screening and for testing of novel cardiac regeneration approaches[26–28]. However, as their typical thickness of 0.2 to 0.5 mm exceeds the scattering length of ballistic photons, single- and even multi-photon microscopes fail to capture sub-cellular information from these slices. To illustrate this limitation, we recorded two-photon microscopy stacks of heart muscle tissue (Fig. 6b). Although the improved penetration depth at the excitation wavelength of 880 nm allows to image significantly deeper than with conventional confocal microscopy, the image contrast degraded quickly with increasing depth, making it impossible to resolve individual sarcomeres (typical spacing, 2 µm) or cell contours beyond a depth of 100 µm. These results are in agreement with previously published contractility studies where the requirement for fast and high-resolution sampling has so far prevented imaging of cellular features in live heart tissue at depths greater than 100 µm[1,7].

To test if microlasers can sense contractility of cardiomyocytes at depths beyond the limit of current microscopes, we applied them to a series of living myocardial slices with varying thickness between 100 and 400 µm (Fig. 6c). To improve light penetration, we changed to red-emitting lasers ($\lambda = 610$ nm) that are pumped by green light ($\lambda = 540$ nm). Although the signal decreased with increasing tissue thickness, sufficient SBRs from 2 pairs of TE and TM modes were obtained to perform full RI analysis even through 400 µm thick cardiac slices (Fig. 6d, Supplementary Fig. 14), i.e. at a depth that was 4 times greater, than the maximum depth at which confocal and multiphoton microscopes can still resolve sub-cellular features. Upon electrical pacing, the slices contracted reproducibly, inducing clearly measurable changes in n_{ext} (Fig. 6e). From this data, we extracted high resolution contractility profiles (Fig. 6f), comparable in quality and amplitude to those detected in isolated CMs (c.f. Fig. 5c).

Discussion

Restoring cardiac function after severe heart injury remains a major clinical challenge due to the low capacity of the adult mammalian heart to grow new CMs[29]. Current regeneration approaches explore the injection of CMs derived from human embryonic stem cells (hESC) or induced pluripotent stem cells (hiPSC) into the injured heart and the growth of cardiac tissue *in vitro*[30–33]. Multifunctional probes which monitor engineered cardiac tissue or the long-term integration of injected cells are urgently needed. Chemical sensing with dye-based or transgenic calcium and voltage reporters are now routinely used for all-optical electrophysiology[24,34]. However, despite their importance, these sensors do not provide insights into the mechanical forces developed by the cells. The processes by which engineered and native cardiac tissue couple mechanically therefore remain unknown[31,35]. Microlaser-based contractility measurements fill this critical gap by monitoring the

contractile properties of individual cells during various developmental stages without the need for staining or genetic alteration. Our spectroscopic contractility technique is also resilient to scattering compared to imaging-based methods since scattering in biological tissue is elastic and hence does not alter spectral characteristics. Furthermore, the nanosecond-pulsed pumping in combination with single-shot read-out applied here virtually eliminates temporal averaging effects that represent a common source of motion artefacts in intravital confocal or light sheet microscopy.[6] This can be combined with recent advances in focussing of light deep into scattering tissue[36], to achieve remote and non-invasive monitoring of cardiac function *in vivo*. For the example of cardiac slices shown here, the high sensitivity, bright emission and single cell specificity of the microlasers leads to better performance at depth than achievable with state-of-the-art microscopes. We expect that the application of novel microlaser sources that are excited in the near-infrared transparency windows of biological tissue will enable a dramatic further increase in sensing depth[37].

In the future, implementing our recently developed semiconductor WGM nanolasers[14], nanowire lasers[38,39], or plasmonic nanolasers[40,41] will improve and simplify internalization further, eliminate any mechanical restriction of the laser probes and drastically reduce the required pump energy. However, surface passivation, heat management and advanced calibration protocols are needed for these single mode lasers before a comparable degree of bio-compatibility and RI sensitivity can be achieved. Furthermore, using high throughput chip-based devices[42] can enable massively parallel integration of lasers into hiPSC- or hESC-derived cardiomyocytes which in turn would facilitate labelling and monitoring of individual cells from the very early stages of the generation of functional cardiac tissue onwards. Likewise, microlasers can offer functional sensing in newly developed stem cell therapies that are able to restore infarcted tissue[43]. Moreover, techniques developed for ultra-sensitive detection, including quantum-enhanced single molecule biosensing or frequency comb spectroscopy, might be adopted to increase sensitivity and specificity of intracellular microlaser sensors even further[44–46]. By providing single cell specificity, long-term tracking, and reduced sensitivity to scattering, microlasers introduce new possibilities for translational approaches that extend well beyond current microscopy-based techniques, offer reduced complexity, and impose fewer experimental restrictions.

References

1. Aguirre, A. D., Vinegoni, C., Sebas, M. & Weissleder, R. Intravital imaging of cardiac function at the single-cell level. *Proc. Natl. Acad. Sci.* **111**, 11257–11262 (2014).

2. Kobirumaki-Shimozawa, F. *et al.* Nano-imaging of the beating mouse heart in vivo: Importance of sarcomere dynamics, as opposed to sarcomere length per se, in the regulation of cardiac function. *J. Gen. Physiol.* **147**, 53–62 (2016).

3. Pasqualin, C. *et al.* SarcOptiM for ImageJ: high-frequency online sarcomere length computing on stimulated cardiomyocytes. *Am. J. Physiol. Physiol.* **311**, C277–C283 (2016).

4. Lind, J. U. *et al.* Instrumented cardiac microphysiological devices via multimaterial three-dimensional printing. *Nat. Mater.* **16**, 303–308 (2016).

5. Mickoleit, M. *et al.* High-resolution reconstruction of the beating zebrafish heart. *Nat. Methods* **11**, 919–922 (2014).

6. Vinegoni, C., Lee, S., Aguirre, A. D. & Weissleder, R. New techniques for motion-artifact-free in vivo cardiac microscopy. *Front. Physiol.* **6**, 147 (2015).

7. Matsuura, R. *et al.* Intravital imaging with two-photon microscopy reveals cellular dynamics in the ischeamia-reperfused rat heart. *Sci. Rep.* **8**, 15991 (2018).

8. Liu, R., Li, Z., Marvin, J. S. & Kleinfeld, D. Direct wavefront sensing enables functional imaging of infragranular axons and spines. *Nat. Methods* **16**, 615–618 (2019).

9. Vollmer, F. & Arnold, S. Whispering-gallery-mode biosensing: label-free detection down to single molecules. *Nat. Methods* **5**, 591–596 (2008).

10. Kim, E., Baaske, M. D., Schuldes, I., Wilsch, P. S. & Vollmer, F. Label-free optical detection of single enzyme-reactant reactions and associated conformational changes. *Sci. Adv.* **3**, e1603044 (2017).

11. Schubert, M. *et al.* Lasing within Live Cells Containing Intracellular Optical Microresonators for Barcode-Type Cell Tagging and Tracking. *Nano Lett.* **15**, 5647–5652 (2015).

12. Humar, M. & Yun, S. H. Intracellular microlasers. *Nat. Photonics* **9**, 572–576 (2015).

13. Schubert, M. *et al.* Lasing in Live Mitotic and Non-Phagocytic Cells by Efficient Delivery of Microresonators. *Sci. Rep.* **7**, 40877 (2017).

14. Fikouras, A. H. *et al.* Non-obstructive intracellular nanolasers. *Nat. Commun.* **9**, 4817 (2018).

15. Martino, N. *et al.* Wavelength-encoded laser particles for massively multiplexed cell tagging. *Nat. Photonics* **13**, 720–727 (2019).

16. Liu, P. Y. *et al.* Cell refractive index for cell biology and disease diagnosis: past, present and future. *Lab Chip* **16**, 634–644 (2016).

17. Irving, T. C., Konhilas, J., Perry, D., Fischetti, R. & de Tombe, P. P. Myofilament lattice spacing as a function of sarcomere length in isolated rat myocardium. *Am. J. Physiol. Circ. Physiol.* **279**, H2568–H2573 (2000).

18. Yagi, N. *et al.* Sarcomere-length dependence of lattice volume and radial mass transfer of myosin cross-bridges in rat papillary muscle. *Pflugers Arch. Eur. J. Physiol.* **448**, 153–160 (2004).

19. Moeendarbary, E. *et al.* The cytoplasm of living cells behaves as a poroelastic material. *Nat. Mater.* **12**, 253–261 (2013).

20. Schreckenberg, R. Endogenous Mechanisms for Regulating Myocardial Contractility. in *Cardiomyocytes – Active Players in Cardiac Disease* 135–163 (Springer International Publishing, 2016). doi:10.1007/978-3-319-31251-4_5.

21. Klimas, A. *et al.* OptoDyCE as an automated system for high-throughput all-optical dynamic cardiac electrophysiology. *Nat. Commun.* **7**, 11542 (2016).

22. Dempsey, G. T. *et al.* Cardiotoxicity screening with simultaneous optogenetic pacing, voltage imaging and calcium imaging. *J. Pharmacol. Toxicol. Methods* **81**, 240–250 (2016).

23. Cao, J. & Poss, K. D. Explant culture of adult zebrafish hearts for epicardial regeneration studies. *Nat. Protoc.* **11**, 872–881 (2016).

24. Weber, M. *et al.* Cell-accurate optical mapping across the entire developing heart. *Elife* **6**, e28307 (2017).

25. Brown, D., Samsa, L., Qian, L. & Liu, J. Advances in the Study of Heart Development and Disease Using Zebrafish. *J. Cardiovasc. Dev. Dis.* **3**, 13 (2016).

26. Watson, S. A. *et al.* Preparation of viable adult ventricular myocardial slices from large and small mammals. *Nat. Protoc.* **12**, 2623–2639 (2017).

27. Watson, S. A. *et al.* Biomimetic electromechanical stimulation to maintain adult myocardial slices in vitro. *Nat. Commun.* **10**, 2168 (2019).

28. Fischer, C. *et al.* Long-term functional and structural preservation of precision-cut human myocardium under continuous electromechanical stimulation in vitro. *Nat. Commun.* **10**, 117 (2019).

29. Vujic, A. *et al.* Exercise induces new cardiomyocyte generation in the adult mammalian heart. *Nat. Commun.* **9**, 1659 (2018).

30. Tzahor, E. & Poss, K. D. Cardiac regeneration strategies: Staying young at heart. *Science (80-.).* **356**, 1035–1039 (2017).

31. Shiba, Y. *et al.* Allogeneic transplantation of iPS cell-derived cardiomyocytes regenerates primate hearts. *Nature* **538**, 388–391 (2016).

32. Ronaldson-Bouchard, K. *et al.* Advanced maturation of human cardiac tissue grown from pluripotent stem cells. *Nature* **556**, 239–243 (2018).

33. Liu, Y.-W. *et al.* Human embryonic stem cell–derived cardiomyocytes restore function in infarcted hearts of non-human primates. *Nat. Biotechnol.* **36**, 597–605 (2018).

34. Jones, J. S., Small, D. M. & Nishimura, N. In Vivo Calcium Imaging of Cardiomyocytes in the Beating Mouse Heart With Multiphoton Microscopy. *Front. Physiol.* **9**, 969 (2018).

35. Gaetani, R. *et al.* Epicardial application of cardiac progenitor cells in a 3D-printed gelatin/hyaluronic acid patch preserves cardiac function after myocardial infarction. *Biomaterials* **61**, 339–348 (2015).

36. Jeong, S. *et al.* Focusing of light energy inside a scattering medium by controlling the time-gated multiple light scattering. *Nat. Photonics* **12**, 277–283 (2018).

37. Fernandez-Bravo, A. *et al.* Continuous-wave upconverting nanoparticle microlasers. *Nat. Nanotechnol.* **13**, 572–577 (2018).

38. Feng, C. *et al.* Organic-Nanowire–SiO 2 Core–Shell Microlasers with Highly Polarized and Narrow Emissions for Biological Imaging. *ACS Appl. Mater. Interfaces* **9**, 7385–7391 (2017).

39. Wu, X. *et al.* Nanowire lasers as intracellular probes. *Nanoscale* **10**, 9729–9735 (2018).

40. Hill, M. T. & Gather, M. C. Advances in small lasers. *Nat. Photonics* **8**, 908–918 (2014).

41. Ma, R.-M. & Oulton, R. F. Applications of nanolasers. *Nat. Nanotechnol.* **14**, 12–22 (2019).

42. Wu, Y.-C. *et al.* Massively parallel delivery of large cargo into mammalian cells with light

pulses. *Nat. Methods* **12**, 439–444 (2015).

43. Lee, A. S. *et al.* Prolonged survival of transplanted stem cells after ischaemic injury via the slow release of pro-survival peptides from a collagen matrix. *Nat. Biomed. Eng.* **2**, 104–113 (2018).

44. Mauranyapin, N. P., Madsen, L. S., Taylor, M. A., Waleed, M. & Bowen, W. P. Evanescent single-molecule biosensing with quantum-limited precision. *Nat. Photonics* **11**, 477–481 (2017).

45. Kippenberg, T. J., Holzwarth, R. & Diddams, S. A. Microresonator-Based Optical Frequency Combs. *Science (80-.).* **332**, 555–559 (2011).

46. Coddington, I., Newbury, N. & Swann, W. Dual-comb spectroscopy. *Optica* **3**, 414 (2016).

Acknowledgements

We thank Simon A. Sharples for assistance with the preparation of myocardial slices. This research was financially supported by the European Research Council under the European Union's Horizon 2020 Framework Programme (FP/2014-2020)/ERC Grant Agreement No. 640012 (ABLASE), by EPSRC (EP/P030017/1) and by the RS Macdonald Charitable Trust. S.J.P. acknowledges funding by the Royal Society of Edinburgh (Biomedical Fellowship) and the British Heart Foundation (Grant FS/17/9/32676). SJP and GBR acknowledge support from The Wellcome Trust Institutional Strategic Support Fund to the University of St Andrews (Grant 204821/Z/16/A). M.S. acknowledges funding by the European Commission (Marie Skłodowska-Curie Individual Fellowship, 659213) and the Royal Society (Dorothy Hodgkin Fellowship, DH160102; Grant RGF\R1\180070). Zebrafish embryo sketch created by Lizzy Griffiths and rat sketch copyright by Data Base Center for Life Science (DBCLS).

Author contributions

M.S. designed, performed and analysed laser experiments and imaging. L.W. contributed to lasing experiments and B.C. contributed to sarcomere length measurements. I.R.M.B. and L.W. developed refractive index fitting and peak fitting software, respectively. A.M. and M.S. prepared neonatal CM cultures with support from G.B.M.. G.B.R. prepared isolated CMs and A.D. prepared cardiac slices under supervision of S.J.P.. S.J.P. and M.S. designed physiological experiments in isolated CMs and cardiac slices. C.S.T. supported the preparation of Zebrafish. P.L.A. performed two photon microscopy. M.S. and M.C.G. conceived the project and wrote the manuscript with contributions from all authors.

Competing interests

All authors declare no competing interests.

Additional information

Supplementary information is available for this paper at...

Correspondence and requests for materials should be addressed to M.S. and M.C.G.

Figure Captions

Fig. 1 | Principle of microlaser-based intracellular sensing in neonatal mouse CMs. a, DIC microscopy and **b**, schematic illustration of a group of neonatal CMs and an intracellular microlaser (green sphere). **c**, Magnified view visualizing the contractile movement of the cell around the microlaser due to the action of sarcomeres (dark red fibres). **d**, Measured WGM spectrum of a microlaser showing multi-mode lasing in pairs of TE- and TM-modes (left). WGMs are localized within an equatorial plane close to the surface of the microlaser (inset, green line). Zoom-in onto one peak in the WGM spectrum illustrating the red-shift in lasing wavelength upon CM contraction (right; $\lambda_0 = 519$ nm, $\Delta\lambda = 50$ pm). Scale bar, 15 µm.

Fig. 2 | Transient red-shifts of microlaser emission are caused by changes in intracellular refractive index. a, Contour plot of the temporal evolution of the lasing spectra for an intracellular microlaser, measured with 10 ms temporal resolution. **b**, Magnified view of the areas highlighted in **a**, for a pair of TM (pink) and TE (blue) WGMs. The coloured lines show the centre position of each mode obtained from peak fitting. Shifts to longer wavelengths coincide with spontaneous CM contractions. **c**, Calculated diameter (top) of the microlaser (grey) and time-averaged diameter (green). External refractive index n_{ext} (bottom) calculated with unrestricted microlaser size (grey) and by applying the fixed mean diameter of the microlaser (green). **d**, Typical threshold characteristics (left axis, closed symbols) for the brightest TE mode (blue) and the least intense TM mode (pink) of 4 tracked lasing modes. Lasing thresholds are about 500 µJ/cm² (TE) and 20 mJ/cm² (TM), respectively. Signal-to-background ratio (SBR) (right axis, open symbols) of the same modes under single pulse excitation. **e**, Mode calibration of the 2 modes shown in **b** using data from 6 contractions. From the slope of the linear fit (grey line), a sensitivity *S* of 0.0429 nm^{-1} and 0.0549 nm^{-1} is obtained for the TM and TE mode, respectively. **f**, Continuous single cell monitoring over 10 min (top) at 2 mJ/cm² (corresponding to 2 nJ/pulse) and magnified view of the 20 s window indicated by the red rectangle (bottom). **g**, Average refractive index change (Δn_{ext}) between resting phase (diastole) and peak contraction (systole) for n=12 cells plotted over the corresponding average change of the dominant TE WGM ($\Delta\lambda_{\mathrm{TE}}$). Data representative of more than 20 independent repeats for a total of n>150 cells.

Fig. 3 | Microlasers monitor cellular contractility. 3D arrangement of myofibrils around microlasers in neonatal cardiomyocytes. **a**, Maximum intensity projection showing the sarcomeric protein cTnT (grey), cell nucleus (magenta) and microlaser (green). Scale bar, 15 µm. **b**, Magnified region around the microlaser and **c**, 3D reconstruction of the same area. The microlaser is omitted to show the arrangement of myofibrils more clearly. Scale bar, 10 µm. **d**, Video rate fluorescence microscopy (Supplementary Video 2) of neonatal mouse CMs with labelled myofibrils. Intracellular microlasers are visible as dark circular objects. Scale bars, 5 µm. **e**, Simultaneously acquired temporal profiles of sarcomere length (SL, grey, left axis, extracted from fluorescence profiles of the myofibrils highlighted by the white rectangles in **d**) and n_{ext} (red, right axis, extracted from microlaser spectra). Subfigures labelled according to the images in **d**.

Fig. 4 | Single cell tracking and contractility sensing under compromised conditions. a-d, Microlaser-based tracking and monitoring of a single neonatal CM. **a**, Intracellular n_{ext} trace (green) of an individual CM at start of experiment, and characterized again after 2 h (cyan), 20 h (blue) and 42 h (violet). The black arrow marks increased contractility during spontaneous tachycardia. **b**, Normalized n_{ext} profiles of traces shown in **a** for n=30-40 cell contractions (grey lines), overlaid by the averaged n_{ext} profiles (coloured lines). **c**, Full-width-half-maximum (FWHM) and **d**, average mean contraction time (t_{con}) of the beating profiles in **b**. **e-h**, Effect of nifedipine on single cell contractility. **e**, n_{ext} trace of a spontaneously beating neonatal CM during administration of 500 nM nifedipine (black arrow). **f**, Absolute change in refractive index (Δn_{ext}) recorded before (left, red bar in **e**) and after (right, blue bar in **e**) administration of nifedipine. **g**, Average maximum speed of contraction (contr.) and relaxation (rel.) for the beating profiles shown in **f**. **h**, Peak refractive index change $\Delta n_{\mathrm{ext,\,max}}$ plotted as function of the maximum contraction speed with linear fit to nifedipine data. Also shown is the intermediate region (green bar in **e**). Grey line represents linear fit to the data after equilibration of the cell (blue spheres). All error bars represent s.e.m.

Fig. 5 | Multimodal sensing and *in vivo* integration. a, Extracellular microlaser (white arrow) on top of an adult CM. Scale bar, 30 µm. **b**, Magnified view showing highly organized myofibrils (sarcomere repeat units indicated by dashed blue lines). Scale bar, 4 µm. **c**, Averaged profiles of n_{ext}^{*} (black), SL (blue), and fluorescent calcium reporter (red). Shaded areas represent s.e.m. of at least 10 contractions. Experiments were performed in duplicate for a total of n=5 cells. **d-g**, Integration of microlaser into live zebrafish. **d**, Schematic drawing of microlaser injection. Scale bar, 500 µm. **e**, Microlaser attached to the atrium of a zebrafish heart (3 dpf). Scale bar, 200 µm. **f**, Magnified view of the microlaser (arrow). V, ventricle; A, atrium. Scale bar, 50 µm. **g**, n_{ext} (red spheres) and n_{ext}^{*} (blue line) calculated using sensitivity calibration. 2-4 microlasers were injected into 3 embryos and contraction signals were recorded from 3 microlasers of one embryo.

Fig. 6 | Living myocardial slices and deep tissue contractility sensing. a, Preparation of left ventricular slices from adult rat hearts. Microlasers (red spheres) were deposited on top of contracting slices. Excitation of the microlasers (green arrows illustrate combination of ballistic and diffuse pump light) through the slice and detection of the microlaser emission (red arrows) by the same objective. **b,** Two-photon microscopy images of the left ventricle at different imaging depth (z). Scale bar, 20 µm. **c**, Photograph of precision cut cardiac slices with different thicknesses. Scale bar, 5 mm. **d,** SBR of microlasers as function of slice thickness for the most (TE, blue) and least intense (TM, pink) laser modes. Error bars represent s.e.m., obtained from analysing 2 slices from 2 hearts and 20 microlasers per thickness. **e,** n_{ext} profile of a single microlaser recorded through a 350 µm thick cardiac slice that was electrically paced at 1 Hz. **f,** Overlaid profiles (grey) from **e** and average contractility profile (red). Experiments were performed in triplicate and contractility profiles have been recorded for n=11 microlasers.

Methods

Animals

The use of experimental animals was approved by the Animal Ethics Committee of the University of St Andrews and the University of Edinburgh. The care and sacrifice of animals used conformed to Directive 2010/63/EU of the European Parliament on the protection of animals used for scientific purposes as well as the United Kingdom Animals (Scientific Procedures) Act 1986.

Cell culture

HL-1 cells were cultured in Claycomb medium (Sigma-Aldrich) supplemented with 100 µM norepinephrine, 10 % (v/v) foetal bovine serum (FBS), 2 mM L-glutamine and 1 % (v/v) penicillin/streptomycin (PS). The cells were stored in T-25 flasks (Fisher Scientific) and incubated at 37°C with 5% CO_2. Prior to seeding, the flasks were coated with gelatine/fibronectin (0.02% gelatine, 1 mg/ml fibronectin) for at least an hour to improve adherence of the cells. Cells were supplied daily with 1 ml of medium per 3.5 cm^2 of culture area to maintain and maximise the contractile activity.

Isolation and culture of neonatal cardiomyocytes

Neonatal mouse hearts were obtained from postnatal day 2 – 3 C57 laboratory mice. Tissue was collected, cleaned and cut into pieces in ice-cold calcium- and magnesium-free Dulbecco's phosphate buffered saline and digested for 30 min in papain (10 units/ml; Worthington) at 37°C. Treated tissue was dissociated to a single cell suspension by gentle reverse-pipetting in cell culture medium (Dulbecco's Modified Eagle's Medium with 25 mM glucose and 2 mM Glutamax, 10 % (v/v) FBS, 1 % (v/v) non-essential amino acids, 1 % (v/v) PS). Non-disaggregated material was allowed to sediment for 2 minutes and the cell suspension pelleted by centrifugation at 200 x g for 5 min. Pelleted cells were resuspended in cell culture medium and pre-plated on an uncoated cell culture flask for 2 – 4 h to enrich cardiomyocytes through surface-attachment of fibroblasts. The cell culture medium containing unattached cells was then recovered from this flask, cardiomyocytes concentrated by centrifugation and seeded at a density of 2 x 10^5 cells per dish. Prior to seeding, culture dishes (Ibidi) were coated with 0.02 % gelatin/5 µg/ml fibronectin. Cultures were kept in a humidified incubator at 37°C, 5% CO_2, 95% air. 1 x 10^5 microlasers were added to the dish one day after seeding and incubated over night. Lasing experiments were performed within the next 1-2 days while cultures showed widespread spontaneous contractions for up to two weeks.

Isolation of adult cardiomyocytes

Adult cardiomyocytes were isolated using an adapted Langendorff-free protocol as previously described.[47] Isolation solutions used were based on a modified Tyrode's solution: EDTA buffer (in mM): 5 KCl, 130 NaCl, 0.5 NaH2PO4, 10 HEPES, 10 glucose, 5 Na-pyruvate and 5 ethylenediaminetetraaceticacid (EDTA) titrated to pH 7.8 with NaOH; Perfusion buffer (in mM): 5 KCl, 130 NaCl, 0.5 NaH2PO4, 10 HEPES, 10 glucose, 5 Na-pyruvate and 1 MgCl2 titrated to pH 7.8 with NaOH; Collagenase buffer: 35 mg collagenase type II (Worthington, USA), 50 mg BSA and 15 mg protease (type XIV, Sigma-Aldrich, UK) diluted in 30 ml of perfusion buffer.

Adult C57 mice were killed by cervical dislocation, the chest cavity rapidly opened and descending vessels severed. The right ventricle was injected with 7 ml of EDTA buffer over 1 minute to quickly clear residual blood and stop contraction. The ascending aorta was clamped in situ using haemostatic forceps and the heart excised. The heart was then submerged in EDTA buffer, with a further 10 ml injection of EDTA buffer into the left ventricle over 3 minutes. EDTA buffer was cleared by injection of 3 ml of perfusion buffer into the left ventricle. The heart was then submerged in collagenase buffer, and 30-50 ml of collagenase buffer injected into the left ventricle over 10 minutes. Digestion was taken as complete following a marked reduction in resistance to injection pressure. The digested heart was then transferred to a culture dish containing fresh collagenase buffer and trimmed of any excess non-cardiac tissue. Cardiomyocyte dissociation was completed by gentle trituration using a P1000 pipette. Enzymatic digestion was inhibited by addition of perfusion buffer containing 5 % (v/v) FBS (FBS; Thermo Fisher, UK). Isolated cardiomyocytes were reintroduced to Ca^{2+} by three rounds of 20 minutes sequential gravity settling in perfusion buffer containing 300 µM, 500 µM, and 1 mM $CaCl_2$, respectively. Cells were stained (see below) and subsequently transferred into a culture dish (Ibidi) containing 1 mM Ca^{2+} perfusion buffer. After the cells sedimented, 1 x 10^4 microlasers were added to the dish and lasing experiments were performed within 3 hours of isolation.

Cardiomyocyte staining

Neonatal cardiomyocytes were labelled with 100 nM SiR-actin overnight. Following isolation, adult cardiomyocytes were loaded with 10 µM X-Rhod-1 AM (λ_{ex}= 580 nm, λ_{em}= 602 nm; Thermo Fisher, UK) in perfusion buffer containing 1 mM $CaCl_2$ for 45 minutes at room temperature. Cells were then washed in 1 mM Ca^{2+} perfusion buffer and left for 15 minutes at room temperature to allow de-esterification of X-Rhod-1 AM.

Microlasers

15 µm diameter polystyrene (PS)- divinylbenzene microspheres stained with Firefli Fluorescent Green (Thermo Fisher, UK, 11895052, CV<12%, excitation/emission maximum: 468 nm/508 nm) were used in all experiments, except for cardiac slices where 15.5 µm diameter PS microspheres (MicroParticles GMBH, Germany, PS-FluoRed-15.5, CV 2%, excitation/emission maximum: 530 nm/607 nm) were used.

Laser spectroscopy

All components for optical pumping and laser spectroscopy were integrated into a standard inverted fluorescence microscope (Nikon, TE2000), equipped with epi fluorescence and differential interference contrast (DIC). The output from a Q-switched diode pumped solid state laser (Alphalas) with wavelength, pulse width and repetition rate of 473 nm, 1.5 ns, and 100 Hz, respectively, was coupled into the objective via a dichroic filter and passed to the sample through either a 60x oil immersion (Nikon CFI Plan Apo VC, NA 1.4) or a 40x (Nikon, Plan Apo, NA 0.95) objective. In addition, a further 1.5x magnification was used for sarcomere length tracking. The pump laser was focussed to a 15 µm large spot and a maximum pulse energy of 5-50 nJ was used depending on resonator size and tissue scattering. Emission from the microlaser was collected by the same objective, separated from the pump light by the dichroic and passed to the camera port of the microscope. The image was relayed to a 300 mm spectrometer (Andor Shamrock 303i and Andor Newton DU970P-BVF) and a cooled sCMOS camera (Hamamatsu, Orca Flash 4.0v2) using a series of relay lenses and dichroic beam splitters. The pump laser and spectrometer were synchronized such that each spectrum corresponded to a single pump pulse (i.e. acquisition rate, 100 Hz). We note that in the single pulse excitation and single pulse collection scheme applied here the acquisition rate can be further increased by increasing both, laser repetition frequency and spectrometer acquisition rate. During lasing experiments, cells were kept in a humidified on-stage incubator system (Bioscience Tools) set to 37°C and purged with 5% CO_2, 95% air.

Laser threshold characteristics were acquired on the same setup by varying the pump power with a set of neutral density filters. Below threshold, spectra were integrated over 800 pump pulses while above threshold between 100 and 20 pump pulses were used. The Signal-to-Background ratio (SBR) is defined as: $\mathrm{SBR} = \frac{I_{\mathrm{WGM}} - I_{\mathrm{BG}}}{I_{\mathrm{BG}}}$, where I_{WGM} is the laser mode peak intensity and I_{BG} is the average background intensity in a 1 nm window around the laser mode. SBR measurements were performed by integrating over only 1 pump pulse to resemble the conditions of the cardiac measurements. 100 spectra were analysed for each pump energy.

Cardiac slices were measured on the same microscope. Red-emitting microlasers were pumped by an OPA tuned to 540 nm (Ekspla, 26 ps pulse width, 1kHz repetition rate) through a 20x objective (Nikon, CFI Plan Fluor, NA 0.45). Here the acquisition rate of the spectrometer was 50 Hz. SBR was determined as above, analysing 500 spectra for each microlaser. Contractility data in thick slices were obtained by smoothing (Savitzky-Golay, 15 points, 2nd order) the fitted laser mode time traces before application of the RI fitting algorithm.

Confocal microscopy

Confocal imaging was performed on a Leica TCS SP8 laser scanning microscope with 40× and 63× oil immersion objectives. Neonatal CMs were fixed for 10 min in 4% paraformaldehyde, permeabilized with Triton X-100 (1 h) and subsequently incubated with the primary cardiac troponin T (cTnT) monoclonal antibody (over night at 4°C) (Thermo Fisher, UK, MA5-12960), the secondary Anti-Mouse IgG CF™ 594 antibody (1 h) (Sigma-Aldrich, SAB4600092), and DAPI. DAPI, microlasers and myofibrils were excited by sequentially scanned continuous wave lasers with a wavelength of 405 nm, 488 nm, and 594 nm, respectively.

Multiphoton microscopy

Imaging was carried out on a Zeiss LSM 710 confocal/multiphoton system based on a Zeiss AXIO Observer Z1 inverted microscope equipped with a Plan-Apochromat 20x NA 0.8 objective. Confocal

imaging used a 543 nm CW laser and multi-photon imaging a Coherent Chameleon laser tuned to 880 nm. The sample was stained by Langendorff perfusion of an adult rat heart with a 100 µM solution of the membrane dye Di-2-ANEPEQ (PromoCell, PK-CA707-61013), for 30 min at room temperature, followed by dissection of the left ventricle and subsequent imaging.[1] The power of the multiphoton laser was increased with increasing imaging depth.

Multimodal imaging

In addition to the laser coupling spectroscopy optics, a red bandpass filter placed in the dia illumination path of the microscope, a quad-edge epi-luminescence filter cube and additional band pass filters at the spectrograph and camera allowed simultaneous recording of microlaser lasing spectra, and the epi-fluorescence and DIC imaging of cells. Live cell imaging was performed by using an on-stage incubator system.

Sarcomere length measurements

To determine the average sarcomere length in neonatal mouse cardiomyocytes, myofibrils were fluorescently labelled with SiR-actin (see above) and videos were recorded under epi-illumination conditions at 50 fps using a 60x oil immersion objective (NA 1.4). Raw fluorescence microscopy images were first smoothed by removing statistical noise.[48] From the smoothed videos intensity profiles were taken along individual myofibrils, covering 5 to 8 sarcomere units. Profiles were then interpolated by a factor of 10, to facilitate an increase in the spatial resolution of the length measurements to about 10 nm that was otherwise limited by the pixel size of the camera and magnification of the microscope. Interpolated profiles were smoothed using the Savitzky-Golay method. Minima in the intensity profiles were tracked through time at 20 ms intervals. Once the separation between the first and last minima was determined, it was divided by the number of sarcomeres to calculate the average sarcomere length in each frame. In adult cardiomyocytes, sarcomere length measurements were performed using DIC videos recorded at 100 fps by using the ImageJ plugin SarcOptiM.[3] Briefly, a fast Fourier transformation algorithm is used to extract the regular spacing in a line profile plotted along the longitudinal axis of the cell. Adult cardiomyocytes were electrically paced at 1 Hz with Platinum wire bath electrodes by applying 8 ms square voltage pulses with a maximum electric field of 30 V/cm.

***In vivo* zebrafish experiments**

All zebrafish embryos used in our experiments were under the age of 5 days post fertilisation (dpf). Embryos were collected from random matings and then correctly developmentally staged. Fertilised eggs were transferred at the 2–8 cell stage to 10 cm culture dishes at 28.5°C with systems water replaced every 24 h. When necessary, larvae were anaesthetised with MS-222 (tricaine methanesulfonate, 40 µg/ml, Sigma-Aldrich). Microlasers were injected into the sinus venosus region of 3 dpf embryos with a micropipette (pulled on a Sutter P97) attached to a Narishige IM-300 microinjector, whilst viewed on a stage of a Leica M16F stereo microscope. Lasing experiments were performed at room temperature.

Cardiac slices

Preparation of cardiac slices from rat hearts was previously described.[26,28]

Experimental solutions were as follows: Slicing solution (in mM) – 30 BDM, 140 NaCl, 6 KCl, 10 glucose, 1 $MgCl_2$, 1.8 $CaCl_2$, 23 $NaHCO_3$ titrated to 7.4 with HCl; Tyrode's solution (in mM): 140 NaCl, 5 KCl, 10 glucose, 1 $MgCl_2$, 2 $CaCl_2$, 23 $NaHCO_3$ titrated to 7.4 with HCl. Solutions were filtered with 0.22-micron filter (Millipore) and cooled to 4°C. Carbogen gas (95% O_2/5% CO_2) was used to bubble solutions throughout the preparation and slicing of the heart.

Adult Wistar rats were anesthetised by Pentobarbital injection, sacrificed by cervical dislocation and death confirmed by carotid artery dissection. The chest cavity was opened and the vessels cut. The heart and lungs were removed from the animal, submerged in cold slicing solution and blood ejected from the heart by compressing for 10-15 seconds. Heart and lungs were transferred to a 10 cm dish (Fisher) filled with cold slicing solution. Using a scalpel, the lungs were dissected off, followed by the atria and right ventricle. An incision was made down the septum towards the apex, the ventricle opened, papillary muscles removed and tissue block flattened. Excess solution was blotted from the epicardial surface, and the tissue block attached to a block of 3.5% agar (3.5% agar made in dH_2O) using superglue - epicardial surface face down. The agar block was then glued to the specimen holder and set in the vibratome bath so the ventricle was sliced from base to apex. The vibratome bath was filled with cold slicing solution until the tissue block was fully covered.

Slicing was carried out on Leica VT 1200 vibratome using a stainless steel blade (Wilkinson Sword) which was replaced for each ventricular block. The settings were as follows: amplitude of 2 mm, blade advance of 0.03 mm/s. Slice thickness was varied between 100–400 µm. Once the slice detached from the tissue block, a fine brush was used to transfer the sample to a well of a 6 well plate (Fisher) filled with 4°C Tyrode's solution. The slice was flattened and held down with gauze and a metal washer and the plate kept on ice.

Data availability

The research data underpinning this publication can be accessed at https://doi.org/10.17630/97927f1f-a111-46d0-8d41-038771733b73.[49]

Code availability

The custom-made computer code is available at https://doi.org/10.17630/97927f1f-a111-46d0-8d41-038771733b73.[49]

47. Ackers-Johnson, M. *et al.* A Simplified, Langendorff-Free Method for Concomitant Isolation of Viable Cardiac Myocytes and Nonmyocytes From the Adult Mouse Heart. *Circ. Res.* **119**, 909–20 (2016).

48. Carlton, P. M. *et al.* Fast live simultaneous multiwavelength four-dimensional optical microscopy. *Proc. Natl. Acad. Sci.* **107**, 16016–16022 (2010).

49. Schubert, M. *et al.* Monitoring contractility in single cardiomyocytes and whole hearts with bio-integrated microlasers (dataset). *Univ. St Andrews Res. Portal* (2020) doi:10.17630/97927f1f-a111-46d0-8d41-038771733b73.

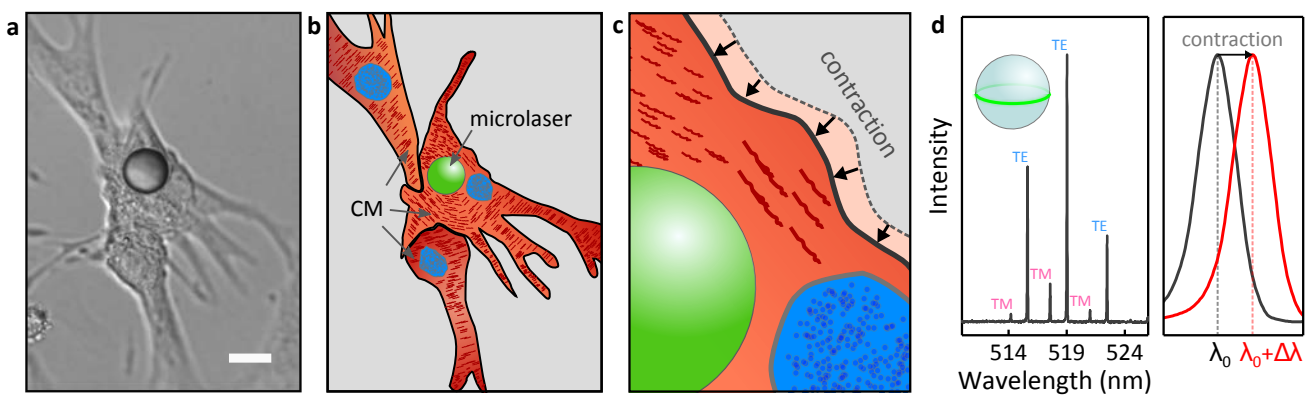
a
b
microlaser
CM
c
contraction
d
TE
TE
TE
TM
TM
TM
Intensity
514
519
524
Wavelength (nm)
contraction
λ0
λ0+Δλ

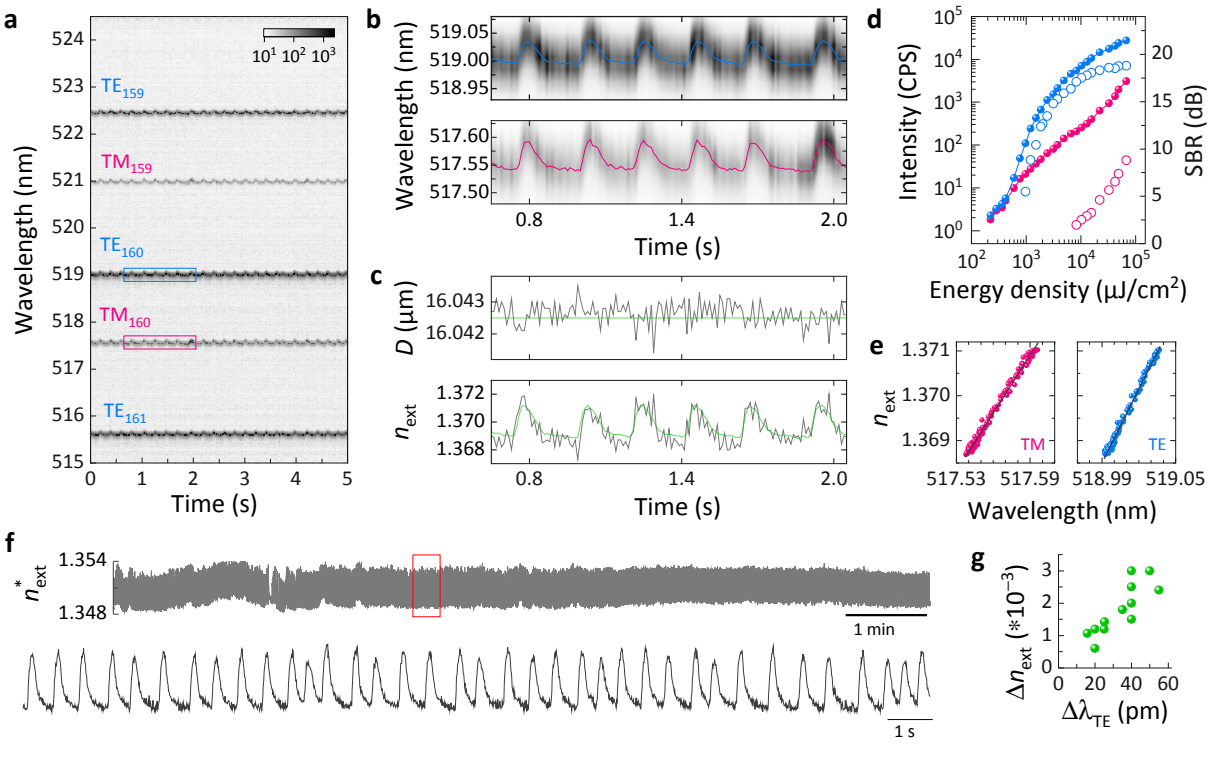
a
Wavelength (nm)
Time (s)
TE159
TM159
TE160
TM160
TE161
b
Wavelength (nm)
Time (s)
c
D (μm)
n_ext
Time (s)
d
Intensity (CPS)
SBR (dB)
Energy density (μJ/cm²)
e
n_ext
TM
TE
Wavelength (nm)
f
n*_ext
1 min
1 s
g
Δn_ext (*10⁻³)
Δλ_TE (pm)

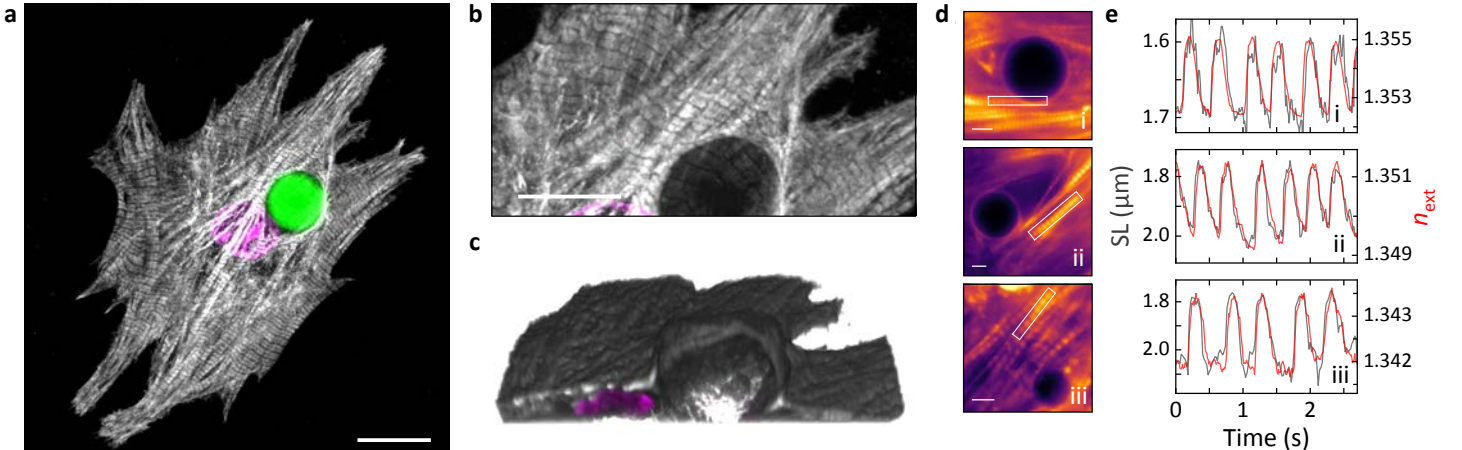
a
b
c
d
e
i
ii
iii
1.6
1.7
1.8
2.0
1.355
1.353
1.351
1.349
1.343
1.342
SL (μm)
n_{ext}
0
1
2
Time (s)

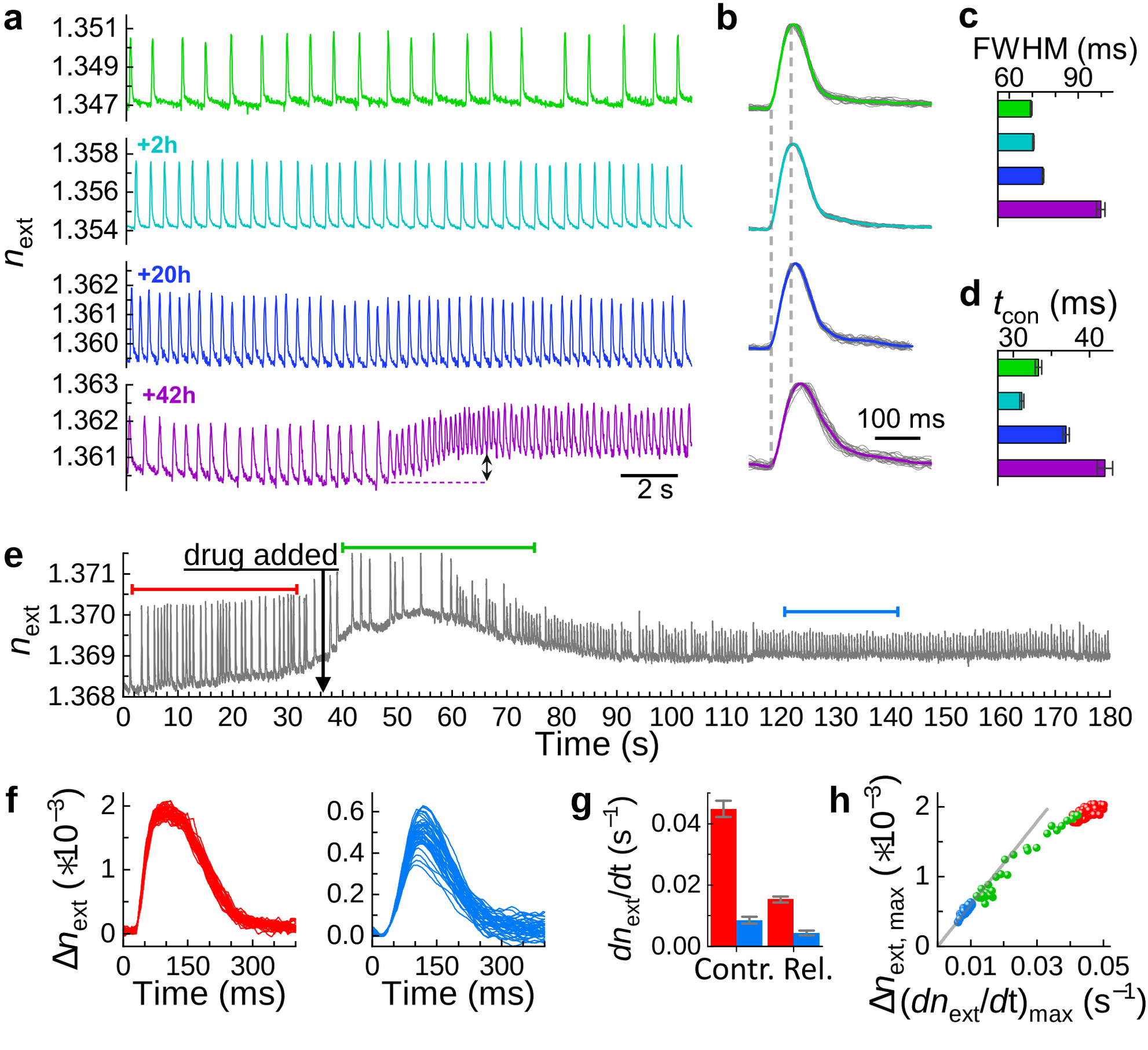
a
b
c
d
e
f
g
h
n_{ext}
1.351
1.349
1.347
+2h
1.358
1.356
1.354
+20h
1.362
1.361
1.360
+42h
1.363
1.362
1.361
2 s
100 ms
FWHM (ms)
60
90
t_{con} (ms)
30
40
drug added
1.371
1.370
1.369
1.368
0 10 20 30 40 50 60 70 80 90 100 110 120 130 140 150 160 170 180
Time (s)
Δn_{ext} ($*10^{-3}$)
2
1
0
0 150 300
Time (ms)
0.6
0.4
0.2
0.0
0 150 300
Time (ms)
dn_{ext}/dt (s^{-1})
0.04
0.02
0.00
Contr. Rel.
$\Delta n_{ext, max}$ ($*10^{-3}$)
2
1
0
0.01 0.03 0.05
$\Delta(dn_{ext}/dt)_{max}$ (s^{-1})

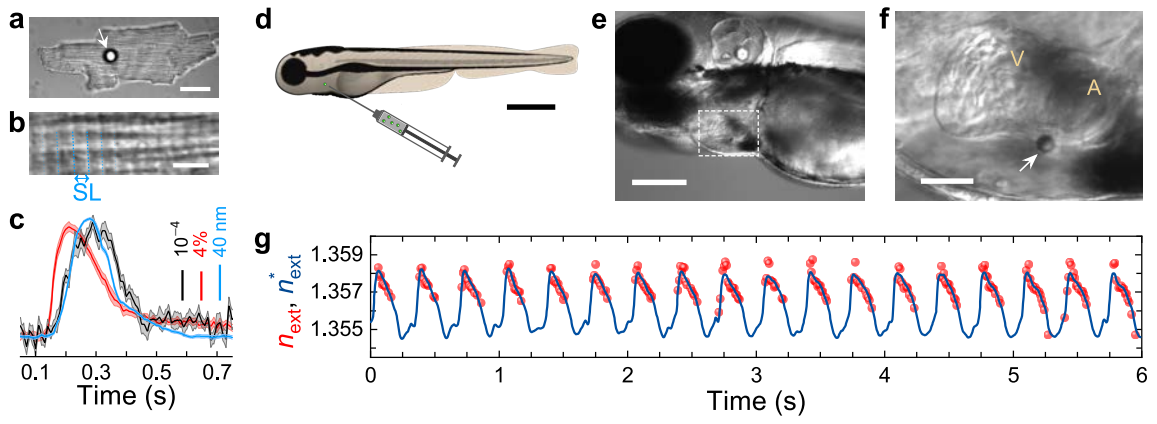
a
b
SL
c
10^{-4}
4%
40 nm
0.1
0.3
0.5
0.7
Time (s)
d
e
f
V
A
g
n_{ext}, n^*_{ext}
1.359
1.357
1.355
0
1
2
3
4
5
6
Time (s)

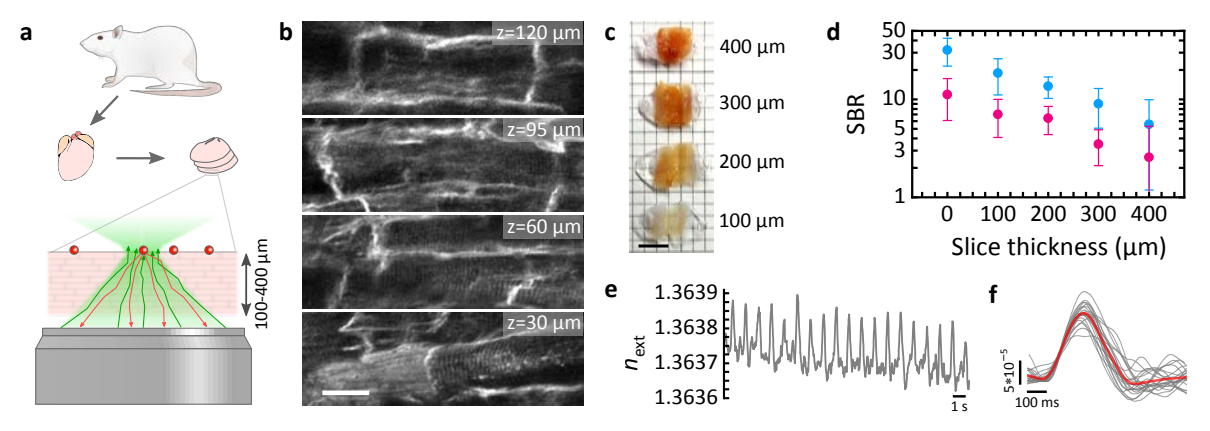
a
100-400 µm
b
z=120 µm
z=95 µm
z=60 µm
z=30 µm
c
400 µm
300 µm
200 µm
100 µm
d
SBR
50
30
10
5
3
1
0
100
200
300
400
Slice thickness (µm)
e
n_{ext}
1.3639
1.3638
1.3637
1.3636
1 s
f
5•10⁻⁵
100 ms